

Edge states of Floquet-Dirac semimetal in a laser-driven semiconductor quantum-well

Boyuan Zhang

University of Tsukuba

Nobuya Maeshima

University of Tsukuba

Ken-ichi Hino (✉ hino@ims.tsukuba.ac.jp)

University of Tsukuba

Article

Keywords: Floquet-Dirac semimetal, laser driven semiconductor quantum-well, edge state

Posted Date: September 9th, 2020

DOI: <https://doi.org/10.21203/rs.3.rs-57853/v1>

License: © ⓘ This work is licensed under a Creative Commons Attribution 4.0 International License.

[Read Full License](#)

Version of Record: A version of this preprint was published at Scientific Reports on February 3rd, 2021.
See the published version at <https://doi.org/10.1038/s41598-021-82230-3>.

1 **Edge states of Floquet-Dirac semimetal in a laser-driven**
2 **semiconductor quantum-well**

3 Boyuan Zhang,¹ Nobuya Maeshima,² and Ken-ichi Hino^{3,2,*}

4 ¹*Doctoral Program in Materials Science,*
5 *Graduate School of Pure and Applied Sciences,*
6 *University of Tsukuba, Tsukuba, Ibaraki 305-8573, Japan*

7 ²*Center for Computational Sciences,*
8 *University of Tsukuba, Tsukuba 305-8577, Japan*

9 ³*Division of Materials Science, Faculty of Pure and Applied Sciences,*
10 *University of Tsukuba, Tsukuba 305-8573, Japan*

11 (Dated: August 12, 2020)

Abstract

Band crossings observed in a wide range of condensed matter systems are recognized as a key to understand low-energy fermionic excitations that behave as massless Dirac particles. Despite rapid progress in this field, the exploration of non-equilibrium topological states remains scarce and it has potential ability of providing a new platform to create unexpected massless Dirac states. Here we show that in a cw-laser driven semiconductor quantum-well, the optical Stark effect conducts bulk-band crossing, and the resulting Floquet-Dirac semimetallic phase supports an unconventional edge state in the projected one-dimensional Brillouin zone. Further, we reveal that this edge state mediates a transition between topological and non-topological edge states that is caused by tuning the laser intensity. The existence of the respective edge states and the related topological numbers are understood in a unified manner in terms of the laser-induced polarization reflecting parity hybridization in the bulk Brillouin zone.

12 The theoretical prediction and the subsequent discovery of topological insulators^{1,2} have
13 led to explosive expansion of the studies of topological perspectives of condensed matter^{3,4}
14 and photonic crystals,⁵ where a sharp distinction between topologically trivial and non-
15 trivial phases with energy gaps is made by the presence of a gapless Dirac dispersion. The
16 viewpoint of the gapless state has been developed to connect to the studies of topological
17 semimetals akin to graphene,⁶ termed Dirac, Weyl, and line-node semimetals.^{7,8} Emergence
18 of topological gapless phases is derived from symmetries inherent in the physical system of
19 concern, namely, the time-reversal (T-)symmetry, the spatial-inversion (I-)symmetry, small
20 groups supported by space groups, and so on.⁷⁻¹⁶ As regards a Dirac semimetal (DSM), this
21 is realized by an accidental band crossing due to fine-tuning of material parameters,^{9,10} the
22 symmetry-enforced mechanism,^{11,12} and the band inversion mechanism.¹³⁻¹⁵ Further, there
23 exist edge modes known as double Fermi arcs at the surface of the DSM formed by the band
24 inversion mechanism.^{15,17-19} Recently, a growing attention has been paid to two-dimensional
25 (2D) DSMs from the perspective of in-depth theories and applications to novel nano scale
26 devices.^{12,16,20-22}

27 While these intriguing topological semimetals are fabricated in equilibrium, there is still
28 concealed attainability of creating and manipulating gapless Dirac dispersions in Floquet
29 topological systems with spatiotemporal periodicity. Owing to this property, the existence
30 of quasienergy bands are ensured by the Floquet theorem.^{23,24} These systems are driven
31 into non-equilibrium states by a temporally periodic external-field that has many degrees
32 of freedom of controlling these states in terms of built-in parameters.²⁵⁻³¹ It is reported
33 that a three-dimensional (3D) DSM, Na₃Bi, is changed to a Floquet-Weyl semimetal by
34 irradiation of femtosecond laser pulses with a circularly polarized light,²⁹ and that band
35 crossings at Dirac points are realized by forming a photonic Floquet topological insulator
36 mimicking a graphene-like honeycomb lattice driven by a circularly polarized light.²⁸ It is
37 remarked that the T-symmetry is broken/protected in a system under the application of a
38 circularly/linearly polarized light-field.

39 In this study, first, we show that a gapless Dirac state emerges in a 2D-bulk band of
40 a semiconductor quantum well driven by a cw-laser with a linear polarization, where the
41 T-symmetry is protected, however, the I-symmetry is broken. Here, the optical Stark effect
42 (OSE) accompanying quasienergy band splitting^{32,33} is introduced to cause an accidental
43 band crossing at high-symmetry points in the 2D Brillouin zone (BZ). This effect is enhanced

44 by a nearly resonant optical excitation from a valence (p -orbital) band to a conduction (s -
 45 orbital), as described later in more detail. Such an optically nonlinear excitation leads to
 46 strong hybridization between the different parity states with s - and p -orbitals over a wide
 47 range of the BZ due to the broken I-symmetry. To the best of one's knowledge, there is
 48 no study thus far in which the OSE is utilized to generate DSM states. Second, we show
 49 that such photoinduced hybridization brings the resulting DSM state to coincide with an
 50 unconventional edge state with a linear and nodeful dispersion in a projected one-dimensional
 51 (1D) BZ. Further, when the laser intensity changes to make a gap open, this edge state is
 52 transformed smoothly into another edge state within this gap; which is either topologically
 53 trivial or non-trivial. Finally, we introduce an interband polarization that reflects the degree
 54 of parity hybridization in the bulk BZ. Based on this, we show that the zero-value contour of
 55 the interband polarization provides the close correspondence between a topological number
 56 of Floquet state in the bulk-BZ and the above-mentioned 1D-edge state irrespective of being
 57 topologically trivial or non-trivial.

58 These edge states concerned here share features with other studies. As regards the OSE, a
 59 valley-selective OSE is demonstrated in monolayer transition metal dichalcogenides with ap-
 60 plication of a circularly polarized electric field.³⁴ As regards edge states of the Floquet DSM
 61 states, Tamm states^{35–37} appearing in the surfaces of several Dirac materials are theoret-
 62 ically examined.³⁸ Recently, growing interest has been captured in the interrelation of Tamm
 63 states with topological edge states in optical waveguide arrays,^{39–42} 1D photonic crystals,^{43–45}
 64 a graphene ring with the Aharonov-Bohm effect,⁴⁶ a honeycomb magnon insulator,⁴⁷ and a
 65 gold surface.⁴⁸

66 Results

Modified Bernevig-Hughes-Zhang model with a laser-electron interaction. We
 begin by constructing the Hamiltonian of the present system of a semiconductor quantum
 well with a linearly polarized light field based on the paradigmatic Bernevig-Hughes-Zhang
 (BHZ) model² composed of two bands with s - and p -orbitals in view of a spin degree of
 freedom. Hereafter, the band with $s(p)$ -orbital is termed as $s(p)$ -band just for the sake of
 simplicity, and the atomic units (a.u.) are used throughout unless otherwise stated. The

BHZ Hamiltonian concerned here is read as the 4×4 -matrix:

$$\mathcal{H}_{\text{BHZ}}(\mathbf{k}) = \epsilon(\mathbf{k})I + \sum_{i=3}^5 d_i(\mathbf{k})\Gamma_i \quad (1)$$

67 with $\mathbf{k} = (k_x, k_y)$ as a 2D Bloch momentum defined in the xy -plane normal to the direction of
 68 crystal growth of quantum well, namely, the z -axis. Here I represents the 4×4 unit matrix,
 69 and Γ_j 's represent the four-dimensional Dirac matrices for the Clifford algebra, defined by
 70 $\Gamma_1 = \tau_x \otimes \sigma_x$, $\Gamma_2 = \tau_x \otimes \sigma_y$, $\Gamma_3 = \tau_x \otimes \sigma_z$, $\Gamma_4 = \tau_z \otimes I_2$, and $\Gamma_5 = \tau_y \otimes I_2$, where I_2 represents
 71 the 2×2 unit matrix, τ_s and σ_s with $s = x, y, z$ represent the Pauli matrices for orbital and
 72 spin degrees of freedom, respectively, and the anti-commutation relation, $\{\Gamma_i, \Gamma_j\} = 2\delta_{ij}$, is
 73 ensured. Further, $\epsilon(\mathbf{k}) = \frac{1}{2}(\epsilon_s + \epsilon_p) - (t_{ss} - t_{pp})(\cos k_x a + \cos k_y a)$, and

$$\begin{cases} d_3(\mathbf{k}) = 2t_{sp} \sin k_y a \\ d_4(\mathbf{k}) = \frac{1}{2}(\epsilon_s - \epsilon_p) - (t_{ss} + t_{pp})(\cos k_x a + \cos k_y a) , \\ d_5(\mathbf{k}) = 2t_{sp} \sin k_x a \end{cases} \quad (2)$$

74 where ϵ_b and $8t_{bb}$ represent the center and width of band b , respectively, and $t_{bb'}$ represents
 75 a hopping matrix between b and $b' (\neq b)$ orbitals with lattice constant a ; after this, a is set
 76 equal to unity. Hereafter, a semiconductor quantum well of HgTe/CdTe is accounted as the
 77 object of material. It is understood that $t_{ss} = t_{pp}$ and $\epsilon_s = -\epsilon_p$. Thus, a Fermi energy is
 78 given by $E_F = (\epsilon_s + \epsilon_p)/2 = 0$, and the energy gap E_g at the Γ -point of the quantum well
 79 equals $2(\epsilon_s - 4t_{ss})$.

An interaction of electron with a laser field is introduced into $\mathcal{H}_{\text{BHZ}}(\mathbf{k})$ by replacing \mathbf{k}
 by $\mathbf{K}(t) = \mathbf{k} + \mathbf{A}(t)$, followed by adding to $\mathcal{H}_{\text{BHZ}}(\mathbf{K}(t))$ an interband dipole interaction
 given by $v(t) = \Omega(t)\Gamma_6$, where $\Gamma_6 = \tau_x \otimes I_2$, and $\Omega(t)$ is a real function of time t , provided
 as $\Omega(t) = \mathbf{F}(t) \cdot \mathbf{X}_{sp}$. Here an electric field of the cw-laser with a linear polarization in
 the x -direction is given by $\mathbf{F}(t) = (F_x \cos \omega t, 0, 0)$ with a constant amplitude F_x and a
 frequency ω , where this is related with a vector potential $\mathbf{A}(t)$ as $\mathbf{F}(t) = -\dot{\mathbf{A}}(t)$, and
 $\mathbf{X}_{sp} = (X_{sp}, 0, 0)$ represents a matrix element of electric dipole transition between s - and p -
 orbitals, independent of \mathbf{k} : $\mathbf{X}_{sp} = \mathbf{X}_{ps}^*$. Thus, in place of $\mathcal{H}_{\text{BHZ}}(\mathbf{k})$, the resulting expression
 ends with up

$$H(\mathbf{k}, t) = \mathcal{H}_{\text{BHZ}}(\mathbf{K}(t)) + v(t) \equiv \sum_{i=3}^6 D_i(\mathbf{k}, t)\Gamma_i, \quad (3)$$

80 where $D_i(\mathbf{k}, t) = d_i(\mathbf{K}(t))$ for $i \neq 6$, and $D_6(\mathbf{k}, t) = \Omega(t)$. Obviously, this ensures the

81 temporal periodicity, $H(\mathbf{k}, t + T) = H(\mathbf{k}, t)$, with $T = 2\pi/\omega$, and the system of concern
 82 follows the Floquet theorem.

83 **T- and pseudo-I-symmetries.** It is evident that the T- and I-symmetries are conserved
 84 in $\mathcal{H}_{\text{BHZ}}(\mathbf{k})$, that is, $\Theta^{-1} \mathcal{H}_{\text{BHZ}}(-\mathbf{k})\Theta = \mathcal{H}_{\text{BHZ}}(\mathbf{k})$, and $\Pi^{-1} \mathcal{H}_{\text{BHZ}}(-\mathbf{k})\Pi = \mathcal{H}_{\text{BHZ}}(\mathbf{k})$, where
 85 Θ and Π represent the T- and I-operators, defined by $\Theta = -iI_2 \otimes \sigma_y K$ and $\Pi = \tau_z \otimes I_2$,
 86 respectively, where K means an operation of taking complex conjugate. Accordingly, by
 87 fine-tuning E_g , it is likely that an accidental band crossing occurs at a high-symmetry point
 88 with four-fold degeneracy.⁹

89 On the other hand, as regards $H(\mathbf{k}, t)$, while the T-symmetry is still respected, the I-
 90 symmetry is broken because $D_i(-\mathbf{k}, t) \neq -D_i(\mathbf{k}, t)$ for $i = 3, 5, 6$, and $D_4(-\mathbf{k}, t) \neq D_4(\mathbf{k}, t)$.
 91 That is, $\Theta^{-1}H(-\mathbf{k}, -t)\Theta = H(\mathbf{k}, t)$, whereas $\Pi^{-1}H(-\mathbf{k}, t)\Pi \neq H(\mathbf{k}, t)$. In fact, it is shown
 92 that in terms of an operator defined as $\tilde{\Pi} = \Pi\mathcal{T}_{1/2}$, the symmetry $\tilde{\Pi}^{-1}H(-\mathbf{k}, t + T/2)\tilde{\Pi} =$
 93 $H(\mathbf{k}, t)$ is retrieved, where $\mathcal{T}_{1/2}$ represents the operation of putting t ahead by a half period
 94 $T/2$, namely, the replacement of $t \rightarrow t + T/2$, and hereafter $\tilde{\Pi}$ is termed as the pseudo-I
 95 operator.

Floquet quasienergy bands. Owing to the Floquet theorem, a wavefunction of the time-
 dependent Schrödinger equation for $H(\mathbf{k}, t)$ is expressed as $\Psi_{\mathbf{k}\alpha}(t)e^{-iE_\alpha(\mathbf{k})t}$ for Floquet state
 α , and thus $\Psi_{\mathbf{k}\alpha}(t)$ is ensured by the quasi-stationary equation

$$L(\mathbf{k}, t)\Psi_{\mathbf{k}\alpha}(t) = E_\alpha(\mathbf{k})\Psi_{\mathbf{k}\alpha}(t) \quad (4)$$

96 under a temporally periodic condition $\Psi_{\mathbf{k}\alpha}(t+T) = \Psi_{\mathbf{k}\alpha}(t)$, where $L(\mathbf{k}, t) = H(\mathbf{k}, t) - iI\partial/\partial t$
 97 and $E_\alpha(\mathbf{k})$ is an eigenvalue termed as quasienergy of the 2D bulk band. It is noted that
 98 $\Theta^{-1}L(-\mathbf{k}, -t)\Theta = L(\mathbf{k}, t)$, and $\tilde{\Pi}^{-1}L(-\mathbf{k}, t + T/2)\tilde{\Pi} = L(\mathbf{k}, t)$. The state α is denoted
 99 as a combination of $\beta(n)$, where β is assigned to either s - or p -band that dominates over
 100 this hybridized state, and n represents an additional quantum number due to the temporal
 101 periodicity that means the number of dressing photons. It is remarked that there is a
 102 relation, $E_{\beta(n+N)}(\mathbf{k}) = E_{\beta(n)}(\mathbf{k}) + N\omega$, with N an integer. Owing to the pseudo-I-symmetry,
 103 $E_\alpha(\mathbf{k})$ equals $E_\alpha(-\mathbf{k})$, where the associated eigenstate of the former is $\Psi_{\mathbf{k}\alpha}(t)$, while that
 104 of the latter is $\tilde{\Pi}\Psi_{\mathbf{k}\alpha}(t) = \Psi_{-\mathbf{k}\alpha}(t + T/2)$. Thus, a component (α', α) of a representation
 105 matrix of $\tilde{\Pi}$ is given by $\frac{1}{T} \int_0^T dt \langle \Psi_{-\mathbf{k}\alpha'}(t) | \Psi_{-\mathbf{k}\alpha}(t + T/2) \rangle$. It is remarked that a parity is
 106 still a good quantum number at a high-symmetry point $\mathbf{k} = \mathbf{k}^j$ ($j = \Gamma, X_1, X_2, M$), that is,

107 $\Pi^{-1}L(\mathbf{k}^j, t)\Pi = L(\mathbf{k}^j, t)$, where four X -points in the 2D-BZ are not equivalent, because the
 108 application of the laser field in the x -direction breaks the C_4 symmetry around the z -axis,
 109 and thus, these are distinguished by representing as X_1 and X_2 .

$E_\alpha(\mathbf{k})$'s are obtained by numerically solving Eq. (4) in the frequency (ω) domain, where the Floquet matrix is recast into $\tilde{L}_{nn'}(\mathbf{k}, \omega) = (n|L(\mathbf{k}, t)|n')$ with respect to n and n' photon states; it is understood that $(n|\cdots|n') = \frac{1}{T} \int_0^T dt e^{-i(n-n')\omega t} \cdots$. The matrix element of it is read as

$$\tilde{L}_{nn'}(\mathbf{k}, \omega) = n\omega\delta_{nn'}I + \sum_{i=3}^6 \tilde{D}_{i,nn'}(\mathbf{k}, \omega)\Gamma_i, \quad (5)$$

110 where $\tilde{D}_{i,nn'}(\mathbf{k}, \omega) = (n|D_i(\mathbf{k}, t)|n')$, and an explicit expression of it is given in Supple-
 111 mentary Note 1. On the other hand, as regards a quasienergy band, $\mathcal{E}_\alpha(k_x)$, which is the
 112 projection of $E_\alpha(\mathbf{k})$ onto the k_x -direction, one applies to Eq. (4) in view of Eq. (5) the
 113 lattice representation in the y -direction where the motion of electron is confined, followed
 114 by solving it under vanishing boundary conditions imposed on two edges.

115 **Quasienergy-band inversion and crossing due to OSE.** Here we show an overall
 116 change of quasienergy spectra with respect to F_x due to the OSE, eventually leading to a
 117 band inversion. Figure 1 shows the scheme of the nearly resonant optical-excitation from the
 118 p -band to s -band with $\omega \lesssim E_g$. Such a scheme of excitation almost maximizes the degree of
 119 the sp hybridization to induce sharp quasienergy-splitting of the order of Ω_R between two
 120 quasienergy bands of $s(n-1)$ and $p(n)$ for $n = 0, 1$, where Ω_R represents the Rabi frequency
 121 given by $F_x X_{sp}$.³² As F_x increases, a pair of photodressed bands of $p(1)$ and $s(-1)$ undergoes
 122 inversion to swerve with anticrossing.

123 Figures 2a and 2b show the calculated results of $\mathcal{E}_{p(1)}(k_x)$ and $\mathcal{E}_{s(-1)}(k_x)$ as a function
 124 of F_x for $k_x = 0$ and π , respectively. It is noted that these bands cross at the abscissa
 125 ($\mathcal{E}(k_x) = E_F = 0$) without anticrossings at F_x 's indicated by I, II, and III; these positions
 126 are mentioned as F_x^I , F_x^{II} , and F_x^{III} , respectively. The band inversions of $p(1)$ and $s(-1)$
 127 discerned in Figs. 2a and 2b accompany the emergence of zero-energy modes indicative of
 128 topological phase transitions, where the zero-energy modes are designated by the horizontal
 129 lines along the abscissa in $F_x^{II} < F_x < F_x^I$ and $F_x < F_x^{III}$, respectively.

130 To examine the band crossings in detail, bulk bands $E(\mathbf{k})$ at F_x^I , F_x^{II} , and F_x^{III} are shown
 131 in Figs. 3a-3c, where $E_{p(1)}(\mathbf{k})$ and $E_{s(-1)}(\mathbf{k})$ are degenerate at a single point of \mathbf{k}^j in the
 132 2D-BZ with $j = \Gamma$, X_2 , and X_1 , respectively; these are indicated in Fig. 3d. Obviously, the

133 crossing points seen in Fig. 2 are found identical with these high-symmetry points projected
 134 on the k_x -axis, which are denoted as $\bar{\Gamma} = \bar{X}_2$ and $\bar{X}_1 = \bar{M}$. Actually, $E(\mathbf{k})$ is conical-
 135 shaped with linear-dispersion in the vicinity of \mathbf{k}^j , and this is considered as a DSM state.
 136 It is understood that hereafter, F_x^I, F_x^{II} , and F_x^{III} are represented as $F_x^\Gamma, F_x^{X_2}$, and $F_x^{X_1}$,
 137 respectively.

138 **Fourfold accidental degeneracy and a σ_z -non-conserving interaction.** Here we
 139 consider the origin of such band crossings. Because of the conservation of both T- and
 140 pseudo-I-symmetries, it is still probable that the band crossing between $p(n)$ and $s(n')$
 141 occurs at a high-symmetry point. In fact, to that end, an additional condition is required
 142 that the difference of photon numbers $\Delta n \equiv n - n'$ is an even number, as is proved rigorously
 143 in Supplementary Note 2. As long as just a single 4×4 -block matrix comprised of two
 144 components, $p(n_0)$ and $s(n'_0 \equiv n_0 - \Delta n)$, for a specific n_0 is concerned in Eq. (5), this
 145 condition is intuitively convinced by seeing that $\tilde{D}_{i,n_0n'_0}(\mathbf{k}^j, \omega) = 0$ with $i = 3, 5, 6$ when Δn
 146 is even — because of odd functions with respect to \mathbf{k} —, as shown in Supplementary Note 1,
 147 and that the remaining term $\tilde{D}_{4,n_0n'_0}(\mathbf{k}^j, \omega)$ is made vanish by fine-tuning F_x . Contrariwise,
 148 when Δn is odd, the resulting pair of bands are gapped out; especially, the two bands $p(1)$
 149 and $s(0)$ never cross. The above-mentioned condition holds exact in general even for $E_{p(1)}(\mathbf{k})$
 150 and $E_{s(-1)}(\mathbf{k})$ that are obtained beyond this simplest two-component model.

Next, we consider the effect of a σ_z -non-conserving interaction on the obtained results,
 which is given by

$$v_z(\mathbf{k}, t) = \sum_{i=1,2} D_i(\mathbf{k}, t) \Gamma_i, \quad (6)$$

151 where $D_i(\mathbf{k}, t) = d_i(\mathbf{K}(t))$, and $d_i(\mathbf{k})$'s are odd functions with respect to \mathbf{k} to keep $v_z(\mathbf{k}, t)$
 152 both T- and pseudo-I-symmetric. Based on the two-component model, when Δn is even, it
 153 is evident that a gap remains closed because of $\tilde{D}_{i,n_0n'_0}(\mathbf{k}^j, \omega) = 0$ with $i = 1, 2$. Similarly
 154 to the above case of the σ_z -conserving interactions, this still hold in general, as is verified in
 155 Supplementary Note 2.

156 **DSM state and edge state.** Here we examine the 1D-band $\mathcal{E}(k_x)$ and a concomitant edge
 157 state that is either topologically trivial or non-trivial; hereafter, it is understood that the
 158 term of the Tamm state³⁸ is used exclusively to mean a trivial state bound on an edge to
 159 distinguish it from a non-trivial one. Figures 4a-4c, 5a-5c, and 6a-6c show the spectra of

160 $\mathcal{E}(k_x)$ in the decreasing order of F_x . It is seen that all the DSM states delimits the boundary
 161 of a topological phase transition (see Figs. 4b, 5b, and 6b). It should be noted that the
 162 DSM states observed at $F_x^{X_2}$ and $F_x^{X_1}$ coincide with edge states with linear and nodeful
 163 dispersions (see Fig. 5b, and Fig 6b, respectively), differing from that observed at F_x^Γ (see
 164 Fig. 4b). Such edge states are termed the Dirac-Tamm state hereafter just for the sake of
 165 convenience of making a distinction from other Tamm states. As regards the Dirac-Tamm
 166 state at $F_x^{X_2}$, with the slight increase of F_x to make a gap open, this is transformed into an
 167 unequivocally topological edge state with its band structure kept almost as it stands (see
 168 Fig. 5a), while with the change of F_x in the opposite direction, this becomes nodeless with
 169 two flat dispersions (see Fig. 5c). As regards the Dirac-Tamm state at $F_x^{X_1}$, with the slight
 170 increase of F_x , this is transformed into a nodeless edge state (see Fig. 6a), while with the
 171 slight decrease of F_x , this becomes unequivocally topologically trivial (see Fig. 6c).

The topological nature of these edge states is evaluated, relying on the bulk-boundary
 correspondence, in terms of the Chern number of state α given by

$$C_\alpha = \frac{1}{2\pi} \oint d\mathbf{k} \cdot \mathbf{a}_\alpha(\mathbf{k}), \quad (7)$$

172 where the Berry connection is defined by $\mathbf{a}_\alpha(\mathbf{k}) = -\frac{i}{T} \int_0^T dt \langle \Psi_{\mathbf{k}\alpha}(t) | \nabla_{\mathbf{k}} \Psi_{\mathbf{k}\alpha}(t) \rangle$. Here, α
 173 is set the lower band, denoted as α_L , where $E_{\alpha_L}(\mathbf{k}) \leq E_F = 0$. It is confirmed that the
 174 non-zero values of $C_{\alpha_L} = 1$ are obtained in $F_x^{X_2} < F_x < F_x^\Gamma$ and $F_x < F_x^{X_1}$, otherwise this
 175 vanishes. Thus, we verify that the edge state observed in $F_x^{X_1} < F_x < F_x^{X_2}$ is a Tamm
 176 state. Further, the Dirac-Tamm states at $F_x^{X_1}$ and $F_x^{X_2}$ are also considered Tamm states,
 177 since their respective net Chern numbers are zero.⁸ To the best of one's knowledge regarding
 178 edge/surface states of DMS, there exists a theoretical study showing that a nodal surface
 179 state — akin to a Dirac-Tamm state — is supported by a 3D massless Dirac fermion, based
 180 on a two-band model of the Dirac equation.³⁸ Further, it is reported that double Fermi
 181 arcs are formed at the surface of a 3D-DSM phase that is created by the band inversion
 182 mechanism.^{8,15,17-19}

Interband polarization. To deepen the understanding of the two types of edge states,
 namely, the topological edge state and the Tamm state, a macroscopic polarization of the
 present system, that is, an induced dipole moment, is examined. This is given by

$$D_{\mathbf{k}\alpha_L}(t) = \langle \Psi_{\mathbf{k}\alpha_L}(t) | x | \Psi_{\mathbf{k}\alpha_L}(t) \rangle = \sum_{bb'(b \neq b')} [P_{\mathbf{k}\alpha_L}(t)]_{bb'} X_{b'b} \quad (8)$$

183 for state α_L , where x is the x -component of position vector of electron. Here, $P_{\mathbf{k}\alpha_L}(t)$
184 represents the associated microscopic interband polarization corresponding to an off-diagonal
185 element of a reduced density matrix, and $[P_{\mathbf{k}\alpha_L}(t)]_{sp} = [P_{\mathbf{k}\alpha_L}(t)]_{ps}$ because of $X_{sp} = X_{ps}$.⁴⁹
186 The interband polarization in the ω -domain is introduced as: $\tilde{P}_{\mathbf{k}\alpha_L}^{(N)}(\omega) = (0|D_{\mathbf{k}\alpha_L}(t)|N)/X_{sp}$
187 with $\tilde{P}_{\mathbf{k}\alpha_L}^{(-N)}(\omega) = [\tilde{P}_{\mathbf{k}\alpha_L}^{(N)}(\omega)]^*$. Below, we examine $\tilde{\mathcal{D}}(\mathbf{k}) \equiv \text{Re}[\tilde{P}_{\mathbf{k}\alpha_L}^{(1)}(\omega)]$ as a function of \mathbf{k} in
188 the 2D-BZ; neither $\tilde{P}_{\mathbf{k}\alpha_L}^{(N \neq \pm 1)}(\omega)$ nor $\text{Im}[\tilde{P}_{\mathbf{k}\alpha_L}^{(\pm 1)}(\omega)]$ show significant variance in the BZ with
189 the change in F_x . It is stated that $\tilde{\mathcal{D}}(\mathbf{k})$ precisely reflects the degree of parity hybridization
190 in the 2D-BZ that results from the I-symmetry breaking due to the laser irradiation.

191 The calculated results of $\tilde{\mathcal{D}}(\mathbf{k})$ are shown in Figs. 4d-4f, Figs. 5d-5f, and Figs. 6d-6f along
192 with $\mathcal{E}(k_x)$ in the vicinity of F_x^Γ , $F_x^{X_2}$, and $F_x^{X_1}$, respectively, where a black solid line shows a
193 contour indicating the boundary of $\tilde{\mathcal{D}}(\mathbf{k}) = 0$, which is hereafter termed as the zero contour.
194 It is readily seen that the zero-contour projected onto the k_x -axis coincides with the segment
195 of the 1D-BZ at which an edge state manifests itself irrespective of being topological or not.
196 To be more specific, the edge state is discerned where a vertical line that is parallel to the
197 k_y -axis at a certain k_x crosses the zero contour twice. For instance, as seen in Fig. 6f, the
198 vertical line crosses this contour twice except around the $\bar{\Gamma}$ -point, and the edge state emerges
199 in the corresponding range of k_x .

200 Another contour indicating $\tilde{\mathcal{D}}(\mathbf{k}) = 0$ is discerned around the M -points in Figs. 4d-
201 4f, which is shown by a black dashed line; this causes no edge state and is attributed to
202 the anticrossing between the bands of $s(-1)$ and $p(2)$. There is a critical difference between
203 $\tilde{\mathcal{D}}(\mathbf{k}^{j^{(c)}})$ with $j^{(c)} = \Gamma, X_2, X_1$ and $\tilde{\mathcal{D}}(\mathbf{k}^M)$ as functions of F_x , as is shown in Fig. 7. A singular
204 nature of $\tilde{\mathcal{D}}(\mathbf{k}^{j^{(c)}})$ is evidently confirmed by seeing that there is discontinuity of $\tilde{\mathcal{D}}(\mathbf{k}^{j^{(c)}})$ at
205 $F_x = F_x^{j^{(c)}}$, namely, $\tilde{\mathcal{D}}(\mathbf{k}^{j^{(c)}})|_{F_x \rightarrow F_x^{j^{(c)}} + 0} \neq \tilde{\mathcal{D}}(\mathbf{k}^{j^{(c)}})|_{F_x \rightarrow F_x^{j^{(c)}} - 0}$, whereas $\tilde{\mathcal{D}}(\mathbf{k}^M)$ is always a
206 continuous function of F_x even in the vicinity of the anticrossing around the M -point. Such
207 a singularity is attributed to an adiabatic interchange of the constituent of wavefunction
208 $\Psi_{\mathbf{k}\alpha_L}(t)$ between $p(1)$ and $s(-1)$ at $\mathbf{k}^{j^{(c)}}$. This brings $\Psi_{\mathbf{k}\alpha_L}(t)$ to be discontinuous, leading
209 to an abrupt change of parity with the traverse of F_x at $F_x^{j^{(c)}}$. In other words, a diabolic
210 point is formed at $\mathbf{k}^{j^{(c)}}$ as a monopole of Berry curvature,⁵⁰ when a massless Floquet Dirac
211 fermion is created at the closure of gap.

212 **Bulk-edge correspondence and \mathbb{Z}_2 topological number.** Next, we show that the
213 shape of the zero contour in the BZ also enables us to determine whether the state α_L is

214 topological or not. It is appropriate to redefine the zero contour as that appears except
 215 around the M-points. This divides the BZ into two regions, R_I and R_O , where $R_{I/O}$ is
 216 defined as the region with/without the Γ -point inside it. Here, let $\nu_{I/O}$ be the number of
 217 high-symmetry points belonging to $R_{I/O}$ and the first quadrant of the BZ coincidentally,
 218 where $\nu_I + \nu_O = 4$. To be specific, as shown in Figs. 4d-4f, a pinhole (shown by a black
 219 filled circle) emerges at the Γ -point at F_x^Γ as the boundary of the phase transition between
 220 the non-topological state with $\nu_I = 0$ (in $F_x > F_x^\Gamma$) and the topological state with $\nu_I = 1$
 221 (in $F_x^{X_2} < F_x < F_x^\Gamma$). Similarly, as shown in Figs. 5d-5f, the band crossing emerging at
 222 the X_2 -point at $F_x^{X_2}$ changes ν_I by one, leading to the further topological transition to
 223 the new phase with $\nu_I = 2$ (in $F_x^{X_1} < F_x < F_x^{X_2}$). The further change of ν_I to 3 (in
 224 $F_x < F_x^{X_1}$) is caused by the phase transition at the X_1 -point, as shown in Figs. 6d-6f.
 225 Accordingly, it is inferred that a topological index ν of the $\mathbb{Z}_2 = (-)^\nu$ number is given by
 226 $\nu = \nu_I \pmod{2} = \nu_O \pmod{2}$. Therefore, the topology relevant to the shape of the zero
 227 contour provides the bulk-edge correspondence in the system of concern and determines the
 228 topological nature of the Floquet state.

229 Discussion

230 This work shows that the nearly resonant laser-excitation gives rise to the fourfold accidental
 231 degeneracies at the high-symmetry points, and the resulting Floquet DSM states host un-
 232 conventional Dirac-Tamm states that are transformable into either topological edge states or
 233 Tamm states with the change of F_x . A stress is put on the key role of this excitation mecha-
 234 nism maximizing the degree of hybridization of different parity states, though there are few
 235 studies thus far that have mentioned its significance for revealing unexplored topological
 236 nature.²⁶ It should be further stressed that the interband polarization reflecting such parity
 237 hybridization provides the close correspondence between the topological number of Floquet
 238 bulk band α_L and the location of the concomitant edge states in the 1D-BK. Therefore, it
 239 is expected that the interband polarization fulfills a role of the guiding principle of Floquet
 240 engineering^{30,51} for topological materials by means of optical controls using cw lasers.

241 Moreover, the studies on the interrelation between a Tamm state and a topological edge
 242 state have been rapidly noticed, because the state-of-the-art techniques of fabrication of op-
 243 tical waveguide arrays and photonic crystals have made it possible to create both edge states
 244 by mimicking the one-dimensional Su-Schrieffer-Hegger model^{39-42,45,52,53} and more compli-

245 cated systems.^{43,44,46} In this work, both of the edge states are transformed in a continuous
 246 manner as a function of the single parameter F_x without changing the composition and
 247 structure of the system, which draws a sharp distinction from these existing studies. It is
 248 also expected that the present findings make an important contribution of understanding
 249 the interrelation between both edge states from a unified perspective.

250 Finally, we make a couple of comments on this study. First, as F_x increases, it is more
 251 likely that the Floquet bands are somewhat modified by effects of the bandgap renormal-
 252 ization and the Rabi energy renormalization due to the many-body Coulomb interaction.⁴⁹
 253 Second, by using a heavier element leading to a stronger spin-orbit interaction, the anti-
 254 crossing between $p(1)$ and $s(-1)$ is made greater and the edge state formed within this gap
 255 is made more pronounced. Third, it would be hard to experimentally realize the findings ob-
 256 tained here, as it stands, because of the 2D topological materials in non-equilibrium. Time-
 257 and- angle-resolved photoemission spectroscopy and cyclotron resonance are considered as
 258 promising methods under the existing circumstances. The former can resolve photo-induced
 259 band gaps in 3D Floquet topological materials,^{27,54} while the latter makes it possible to
 260 observe a precise band structure of a 2D DSM in the HgTe quantum well with critical
 261 thickness.⁵⁵

262 **Methods**

263 Numerical calculations for a wavefunction $\Psi_{\mathbf{k}\alpha}(t)$ of Floquet state α and the associated
 264 quasienergy $E_\alpha(\mathbf{k})$ are implemented by relying on the Fourier-Floquet expansion of Eq. (4),
 265 followed by diagonalizing the Floquet matrix $\tilde{L}_{nn'}(\mathbf{k}, \omega)$. The explicit expressions of matrix
 266 elements of it are given in Supplementary Note 1. The maximum number of photons (N_p)
 267 incorporated in this calculation is three, namely, $n, n' = -N_p \sim N_p$, and the numerical
 268 convergence is checked by using a greater value of N_p . The following material parameters
 269 in the units of a.u. are employed for actual calculations:⁵⁶ $\epsilon_s = -\epsilon_p = 0.01, t_{ss} = t_{pp} =$
 270 $0.001, t_{sp} = 0.002, a = 12.21$, and $X_{sp} = 34.63$. ω and E_g are set to be 0.0114 and 0.012,
 271 respectively.

272 * hino@ims.tsukuba.ac.jp

- 273 ¹ Kane, C. L. & Mele, E. J. Quantum Spin Hall Effect in Graphene. *Phys. Rev. Lett.* **95** 226801-
274 226804 (2005).
- 275 ² Bernevig, B. A., Hughes T. L. & Zhang, S. C. Quantum Spin Hall Effect and Topological Phase
276 Transition in HgTe Quantum Wells. *Science* **314** 1757-1761 (2006).
- 277 ³ Hasan, M. Z. & Kane, C. L. Topological insulators. *Rev. Mod. Phys.* **82** 3045-3067 (2010).
- 278 ⁴ Qi, X. L. & Zhang, C. H. Topological insulators and superconductors. *Rev. Mod. Phys.* **85**
279 1057-1110 (2011).
- 280 ⁵ Ozawa, T. *et al.* Topological photonics. *Rev. Mod. Phys.* **91** 015006 (87 pages) (2019).
- 281 ⁶ Castro Neto, A. H. *et al.* The electronic properties of graphene. *Rev. Mod. Phys.* **81** 109-162
282 (2009).
- 283 ⁷ Wehling; T. O., Black-Schaffer, A. M. & Balatsky, A. V. Dirac materials. *Advances in Physics*
284 **63** 1-76 (2014).
- 285 ⁸ Armitage, N. P. & Mele E. J. Weyl and Dirac semimetals in three-dimensional solids. *Rev. Mod.*
286 *Phys.* **90** 015001 (63 pages) (2018).
- 287 ⁹ Murakami, S. *et al.* Tuning phase transition between quantum spin Hall and ordinary insulating
288 phases. *Phys. Rev. B* **76** 205304 (6 pages) (2007).
- 289 ¹⁰ Murakami, S. Phase transition between the quantum spin Hall and insulator phases in 3D:
290 emergence of a topological gapless phase. *New J. Phys.* **9** 356 (15 pages) (2007); Corrigendum.
291 *New J. Phys.* **10** 029802 (2 pages) (2008).
- 292 ¹¹ Young, S. M. *et al.* Dirac Semimetal in Three Dimensions. *Phys. Rev. Lett.* **108** 140405 (5
293 pages) (2012).
- 294 ¹² Young, S. M. & Kane, C. L. Dirac Semimetals in Two Dimensions. *Phys. Rev. Lett.* **115** 126803(
295 5 pages) (2015).
- 296 ¹³ Wang, Z. *et al.* Dirac semimetal and topological phase transitions in A₃Bi (A = Na, K, Rb).
297 *Phys. Rev. B* **85** 195320 (5 pages) (2012).
- 298 ¹⁴ Wang, Z. *et al.* Three-dimensional Dirac semimetal and quantum transport in Cd₃As₂. *Phys.*
299 *Rev. B* **88** 125427 (6 pages) (2013).
- 300 ¹⁵ Yang, B. -J. & Nagaosa, N. Classification of stable three-dimensional Dirac semimetals with
301 nontrivial topology. *Nat. Comm.* **5** 4898 (10 pages) (2014).
- 302 ¹⁶ Park, S. & Yang, B. -J. Classification of accidental band crossings and emergent semimetals in
303 two-dimensional noncentrosymmetric systems. *Phys. Rev. B* **96** 125127 (13 pages) (2017).

- 304 ¹⁷ Yi, H. *et al.* Evidence of Topological Surface State in Three-Dimensional Dirac Semimetal
305 Cd_3As_2 . *Sci. Rep.* **4** 6106 (6 pages) (2014).
- 306 ¹⁸ Xu, S. -Y. *et al.* Discovery of a Weyl fermion semimetal and topological Fermi arcs. *Science*
307 **349** 613-617 (2015).
- 308 ¹⁹ Kargariana, M., Randeria, M. & Lu, Y. -M. Are the surface Fermi arcs in Dirac semimetals
309 topologically protected?. *PNAS* **113** 86488652 (2016).
- 310 ²⁰ Doh, H. & Choi, H. J. Dirac-semimetal phase diagram of two-dimensional black phosphorus.
311 *2D Mater.* **4** 025071 (8 pages) (2017).
- 312 ²¹ Ramankutty, S. V. *et al.* Electronic structure of the candidate 2D Dirac semimetal SrMnSb_2 : a
313 combined experimental and theoretical study. *SciPost Phys.* **4** 010 (25 pages) (2018).
- 314 ²² Luo, W. *et al.* Two-dimensional Topological Semimetals Protected by Symmorphic Symmetries.
315 *Phys. Rev. B* **101** 195111 (25 pages) (2020).
- 316 ²³ Shirley, J. H. Solution of the Schrödinger Equation with a Hamiltonian Periodic in Time. *Phys.*
317 *Rev.* **138** B979-B987 (1965).
- 318 ²⁴ Kitagawa, T., Berg, E., Rudner, M. & Demler, E. Topological characterization of periodically
319 driven quantum systems. *Phys. Rev. B* **82** 235114 (12 pages) (2010).
- 320 ²⁵ Zhenghao, G. *et al.* Floquet Spectrum and Transport through an Irradiated Graphene Ribbon.
321 *Phys. Rev. Lett.* **107**, 216601-216605 (2011).
- 322 ²⁶ Lindner, N. H., Refael, G. & Galitski, V. Floquet topological insulator in semiconductor quan-
323 tum wells. *Nat. Phys.* **7** 490-495 (2011).
- 324 ²⁷ Wang, Y. H., H. Steinberg, H., Jarillo-Herrero, P. & Gedik, N. Observation of Floquet-Bloch
325 States on the Surface of a Topological Insulator. *Science* **342** 453-457 (2013).
- 326 ²⁸ Rechtsman, M. C. *et al.* Photonic Floquet topological insulators. *Nature* **496** 196-200 (2013).
- 327 ²⁹ Hübener, H. *et al.* Creating stable FloquetWeyl semimetals by laser-driving of 3D Dirac mate-
328 rials. *Nat. Comm.* **8** 13940 (8 pages) (2016).
- 329 ³⁰ Hansen, M. *et al.* Topological edge-state engineering with high-frequency electromagnetic radi-
330 ation. *Phys. Rev. B* **96** 205127 (9 pages) (2017).
- 331 ³¹ Nakagawa, M., Slager, R. -J., Higashikawa, S. & Oka, T. Wannier representation of Floquet
332 topological states. *Phys. Rev. B* **101** 075108 (16 pages) (2020).
- 333 ³² Autler, S. H. & Townes, C. H. Stark Effect in Rapidly Varying Fields. *Phys. Rev.* **100** 703-722
334 (1955).

- 335 ³³ Knight, P. L. & Milonni, P. W. The Rabi frequency in optical spectra. *Phys. Rep.* **66**, 21-107
336 (1980).
- 337 ³⁴ Sie, E. J. *et al.* Valley-selective optical Stark effect in monolayer WS₂. *Nat. Mat.* **14** 290-294
338 (2015).
- 339 ³⁵ Tamm, I. On the possible bound states of electrons on a crystal surface. *Phys. Z. Sov. Union* **1**
340 733-746 (1932).
- 341 ³⁶ Shockley, W. On the Surface States Associated with a Periodic Potential. *Phys. Rev.* **56** 317-323
342 (1939).
- 343 ³⁷ Ohno, H. *et al.* Observation of "Tamm States" in Superlattices. *Phys. Rev. Lett.* **64**, 2555-2558
344 (1990).
- 345 ³⁸ Volkov, V. A. & Enaldiev, V. V. Surface States of a System of Dirac Fermions: A Minimal
346 Model. *J. Exp. Theor. Phys* **122** 608-620 (2016).
- 347 ³⁹ Longhi, S. Zak phase of photons in optical waveguide lattices. *Opt. Lett.* **38** 3716-3719 (2013).
- 348 ⁴⁰ Wang, L. *et al.* Zak phase and topological plasmonic Tamm states in one-dimensional plasmonic
349 crystals. *Opt. Express* **26** 28963-28975 (2018).
- 350 ⁴¹ Chen, T. *et al.* Distinguishing the Topological Zero Mode and Tamm Mode in a Microwave
351 Waveguide Array. *Ann. Phys. (Berlin)* **531** 1900347 (5 pages)(2019).
- 352 ⁴² Yang, Y. & Pan, Y. Engineering Zero Modes, Fano Resonance, and Tamm Surface States in
353 the Waveguide-Array Realization of the Modified Su-Schrieffer-Heeger Model. *Opt. Express* **27**
354 32900-32911 (2019).
- 355 ⁴³ Tsurimaki, Y. *et al.* Topological Engineering of Interfacial Optical Tamm States for Highly
356 Sensitive Near-Singular-Phase Optical Detection. *ACS Photonics* **5** 929 – 938 (2018).
- 357 ⁴⁴ Lu, H. *et al.* Topological insulator based Tamm plasmon polaritons. *APL Photonics* **4** 040801
358 (7 pages) (2019).
- 359 ⁴⁵ Henriques, J. C. G. *et al.* Topological Photonic Tamm-States and the Su-Schrieffer-Heeger
360 Model. *Phys. Rev. A* **101** 043811 (13 pages) (2020).
- 361 ⁴⁶ Latyshev, Y. I. *et al.* Transport of Massless Dirac Fermions in Non-topological Type Edge
362 States. *Sci. Rep.* **4** 7578 (6 pages) (2014).
- 363 ⁴⁷ Pantaléon, P. A., Carrillo-Bastos, R & Xian, Y. Topological Magnon Insulator with a Kekulé
364 Bond Modulation. *J. Phys: Cond. Mat.* **31** 085802 (8 pages) (2019).
- 365 ⁴⁸ Yan, B. Topological states on the gold surface. *Nat. Commun.* **6** 10167(6 pages) (2015).

- 366 ⁴⁹ Haug, H. & Koch, S. W. *Quantum Theory of the Optical and Electronic Properties of Semicon-*
367 *ductors*. Chaps. 12 and 15 (World Scientific, fifth edition, 2009).
- 368 ⁵⁰ Berry M.V. Aspects of Degeneracy. In: Casati G. (eds) *Chaotic Behavior in Quantum Systems*.
369 *NATO ASI Series (Series B: Physics)* **120** 123-140 (Springer, Boston, MA, 1985).
- 370 ⁵¹ Kennes, D. M. *et al.* Floquet Engineering in Quantum Chains. *Phys. Rev. Lett.* **120** 127601 (5
371 pages) (2018).
- 372 ⁵² Su, W. P., Schrieffer, J. R. & Heeger, A. Soliton excitations in polyacetylene. *Phys. Rev. B* **22**
373 2099-2111 (1980).
- 374 ⁵³ Heeger, A. J., Kivelson, S. Schrieffer, J. R. & Su, W. P. Solitons in conducting polymers. *Rev.*
375 *Mod. Phys.* **60** 781-850 (1988).
- 376 ⁵⁴ Sobota, J. A. *et al.* Ultrafast Optical Excitation of a Persistent Surface-State Population in the
377 Topological Insulator Bi₂Se₃. *Phys. Rev. Lett.* **108** 117403 (5 pages) (2012).
- 378 ⁵⁵ Shuvaev, A. M. *et al.* Band Structure of Two-dimensional Dirac Semimetal from Cyclotron
379 Resonance. *Phys. Rev. B* **96** 155434 (7 pages) (2017).
- 380 ⁵⁶ Novik, E. G. *et al.* Band structure of semimagnetic Hg_{1-y}Mn_yTe quantum wells. *Phys. Rev. B*
381 **72** 035321 (12 pages) (2005).

382 **Acknowledgments**

383 This work was supported by JSPS KAKENHI Grant No. JP19K03695. The authors are
384 grateful to Prof. J. Fujioka for fruitful discussion.

385 **Competing financial interests**

386 The authors declare no competing financial interests.

387 **Author contributions**

388 K.H. conceived the main ideas and supervised the project. B.Z. carried out the main parts
389 of the numerical calculations, and N.M. carried out the rest parts of them. All authors
390 discussed and interpreted the results. K.H. wrote the paper and B.Z. prepared the figures
391 with contribution from all authors.

392 **Additional information**

393 Supplementary information is available for the paper at <https://xxx>. Correspondence and
394 requests for materials should be addressed to K.H.

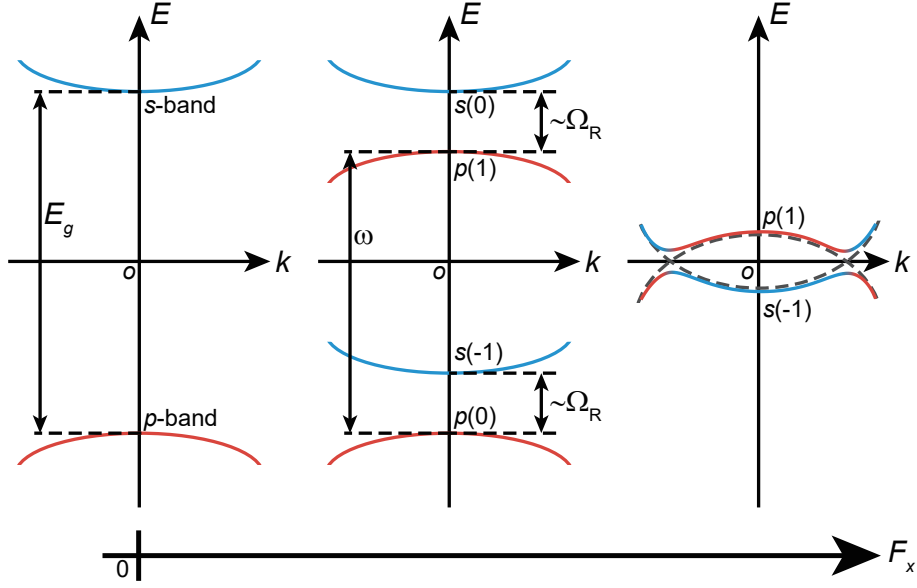


FIG. 1. **Scheme of the nearly resonant optical-excitation followed by the OSE.** (Left) The original energy allocation of the p -band (red solid line) and the s -band (blue solid line) with energy gap E_g . (Center) With the application of cw-laser with frequency ω and constant electric field F_x , the OSE causes quasienergy-splitting of the order of the Rabi frequency Ω_R between a pair of photodressed bands, $s(n-1)$ and $p(n)$, with $n = 0, 1$. (Right) With the further increase in F_x , a pair of bands of $p(1)$ and $s(-1)$ undergoes inversion with anticrossing. Band crossing takes place at a certain F_x , as shown by a dashed line.

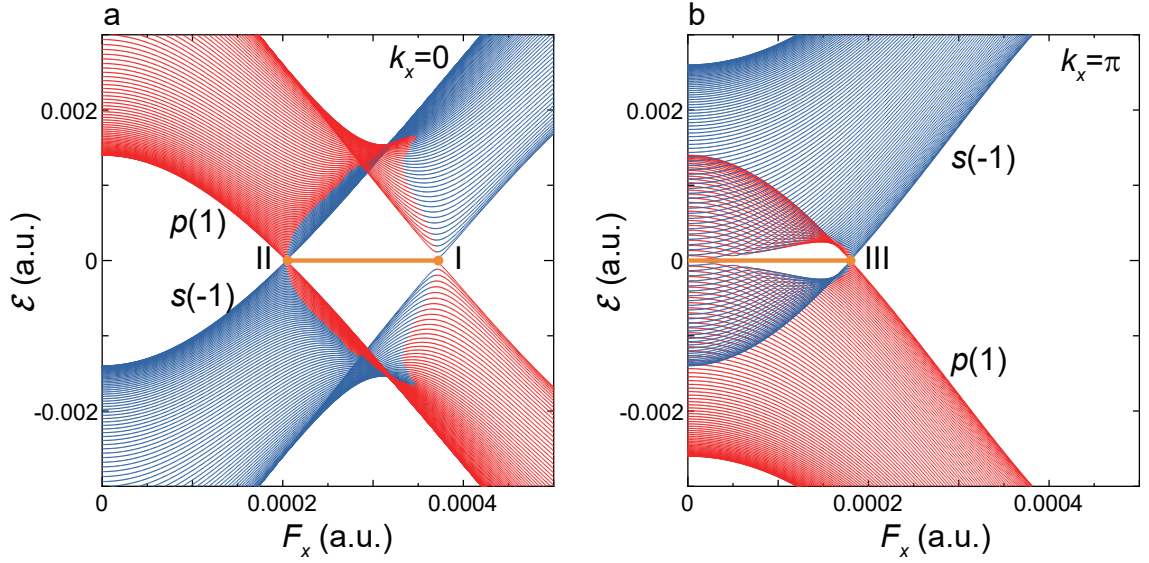


FIG. 2. **Band inversion and band crossing.** (a) Shown are $\mathcal{E}_{p(1)}(k_x)$ and $\mathcal{E}_{s(-1)}(k_x)$ for $k_x = 0$ as a function of F_x . The two quasienergy bands $p(1)$ and $s(-1)$ (shown by red and blue lines, respectively) cross when F_x is fine-tuned at the positions of I and II. Shown are the zero modes (Dirac nodes) by a yellow solid line. (b) The same as the panel (a) but for $k_x = \pi$. The two quasienergy bands cross when F_x is fine-tuned at the position of III.

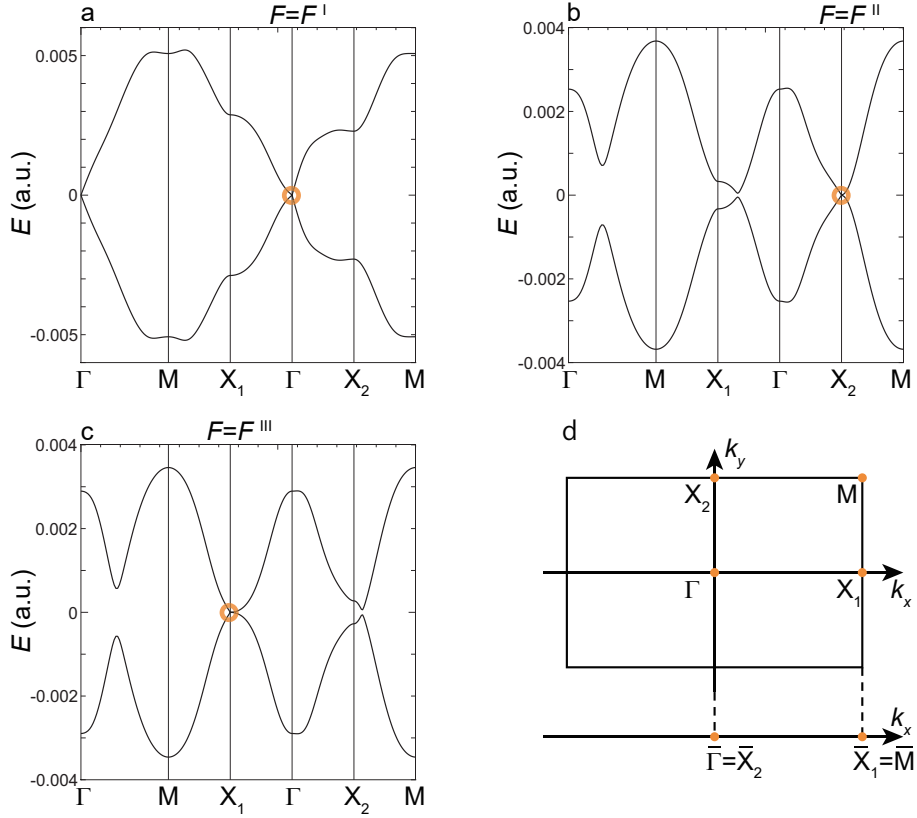


FIG. 3. **Quasienergy dispersion of 2D-bulk band $E(\mathbf{k})$.** (a) Shown is $E(\mathbf{k})$ at F_x^I , where $E_{p(1)}(\mathbf{k})$ and $E_{s(-1)}(\mathbf{k})$ are degenerate at the Γ point. (b) The same as the panel (a) but at F_x^{II} with the degeneracy at the X_2 point. (c) The same as the panel (a) but at F_x^{III} with the degeneracy at the X_1 point. (d) Shown are the high-symmetry points of Γ , X_2 , X_1 and M in the 2D-BZ with their projection onto the k_x -axis denoted as $\bar{\Gamma}$, \bar{X}_2 , \bar{X}_1 and \bar{M} , respectively.

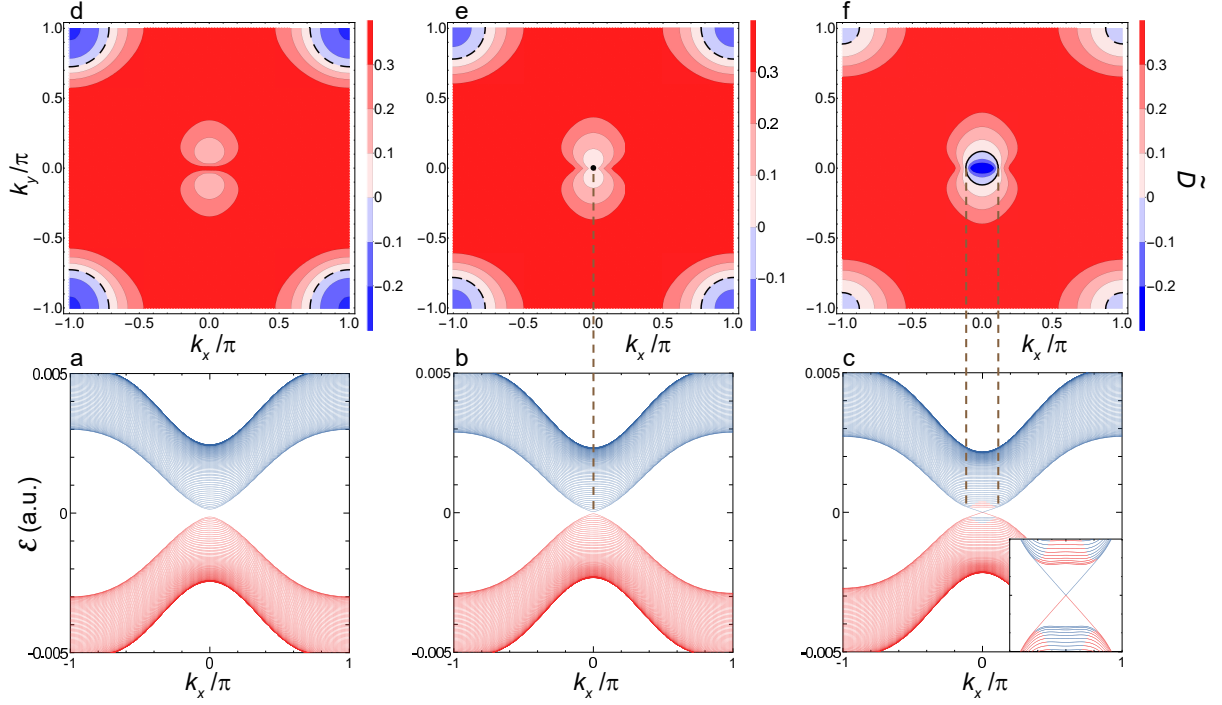


FIG. 4. **Quasienergy dispersion of $\mathcal{E}(k_x)$ and interband polarization $\tilde{\mathcal{D}}(\mathbf{k})$ in the vicinity of F_x^Γ .** (a) Shown are $\mathcal{E}_{p(1)}(k_x)$ and $\mathcal{E}_{s(-1)}(k_x)$ as functions of k_x at $F_x > F_x^\Gamma$. The two quasienergy bands $p(1)$ and $s(-1)$ are shown by red and blue lines, respectively. (b) The same as the panel (a) but at F_x^Γ . (c) The same as the panel (a) but at $F_x < F_x^\Gamma$. Inset: the expanded view of these two bands in the vicinity of the $\bar{\Gamma}$ -point. (d) Shown is a contour map $\tilde{\mathcal{D}}(\mathbf{k})$ in the (k_x, k_y) -plane at $F_x > F_x^\Gamma$. Contours indicating the boundary of $\tilde{\mathcal{D}}(\mathbf{k}) = 0$ are shown by black dashed lines. (e) The same as the panel (d) but at F_x^Γ . Besides, a pinhole indicating $\tilde{\mathcal{D}}(\mathbf{k}) = 0$ at the Γ -point is shown by a black filled circle. The vertical dashed line shows the projection of $\tilde{\mathcal{D}}(\mathbf{k}) = 0$ (the pinhole) onto the k_x -axis shown in the panel (b). (f) The same as the panel (d) but at $F_x < F_x^\Gamma$. Contours indicating the boundary of $\tilde{\mathcal{D}}(\mathbf{k}) = 0$ are shown by black solid and dashed lines. The vertical dashed lines show the projection of $\tilde{\mathcal{D}}(\mathbf{k}) = 0$ (the zero contour) onto the k_x -axis shown in the panel (c).

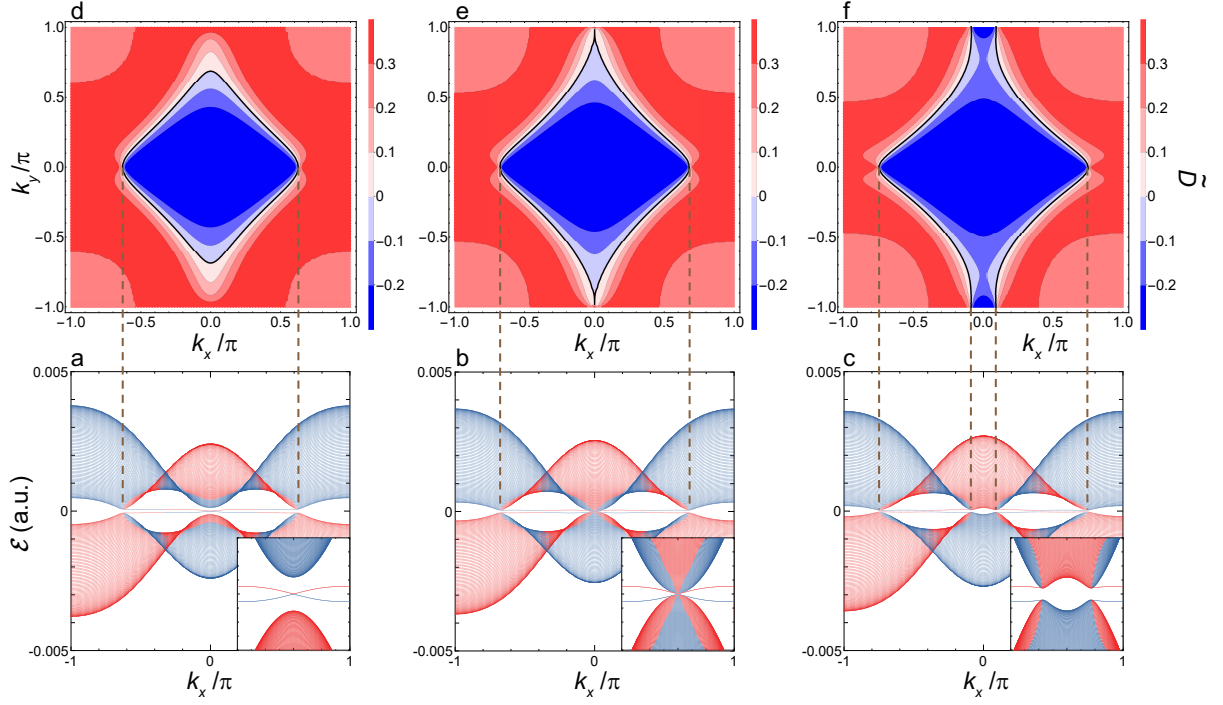


FIG. 5. Quasienergy dispersion of $\mathcal{E}(k_x)$ and interband polarization $\tilde{\mathcal{D}}(\mathbf{k})$ in the vicinity of $F_x^{X_2}$. (a) Shown are $\mathcal{E}_{p(1)}(k_x)$ and $\mathcal{E}_{s(-1)}(k_x)$ as functions of k_x at $F_x > F_x^{X_2}$. The two quasienergy bands $p(1)$ and $s(-1)$ are shown by red and blue lines, respectively. Inset: the expanded view of these two bands in the vicinity of the \bar{X}_2 -point. (b) The same as the panel (a) but at $F_x^{X_2}$. (c) The same as the panel (a) but at $F_x < F_x^{X_2}$. (d) Shown is a contour map $\tilde{\mathcal{D}}(\mathbf{k})$ in the (k_x, k_y) -plane at $F_x > F_x^{X_2}$. The vertical dashed lines show the projection of $\tilde{\mathcal{D}}(\mathbf{k}) = 0$ (the zero contour) onto the k_x -axis shown in the panel (a). (e) The same as the panel (d) but at $F_x^{X_2}$ and with the zero contour projected onto the k_x -axis shown in the panel (b). (f) The same as the panel (d) but at $F_x < F_x^{X_2}$ and with the zero contour projected onto the k_x -axis shown in the panel (c).

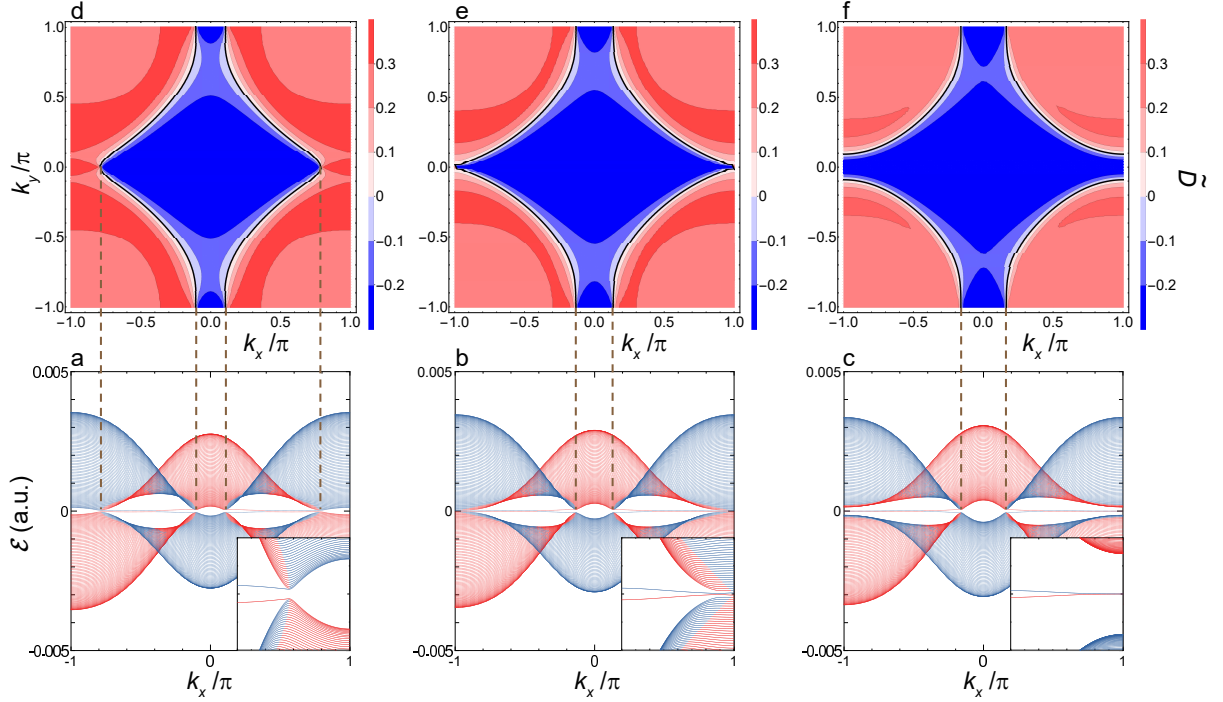


FIG. 6. Quasienergy dispersion of $\mathcal{E}(k_x)$ and interband polarization $\tilde{\mathcal{D}}(\mathbf{k})$ in the vicinity of $F_x^{X_1}$. (a) Shown are $\mathcal{E}_{p(1)}(k_x)$ and $\mathcal{E}_{s(-1)}(k_x)$ as functions of k_x at $F_x > F_x^{X_1}$. The two quasienergy bands $p(1)$ and $s(-1)$ are shown by red and blue lines, respectively. Inset: the expanded view of these two bands in the vicinity of the \bar{X}_1 -point. (b) The same as the panel (a) but at $F_x^{X_1}$. (c) The same as the panel (a) but at $F_x < F_x^{X_1}$. (d) Shown is a contour map $\tilde{\mathcal{D}}(\mathbf{k})$ in the (k_x, k_y) -plane at $F_x > F_x^{X_1}$. The vertical dashed lines show the projection of $\tilde{\mathcal{D}}(\mathbf{k}) = 0$ (the zero contour) onto the k_x -axis shown in the panel (a). (e) The same as the panel (d) but at $F_x^{X_1}$ and with the zero contour projected onto the k_x -axis shown in the panel (b). (f) The same as the panel (d) but at $F_x < F_x^{X_1}$ and with the zero contour projected onto the k_x -axis shown in the panel (c).

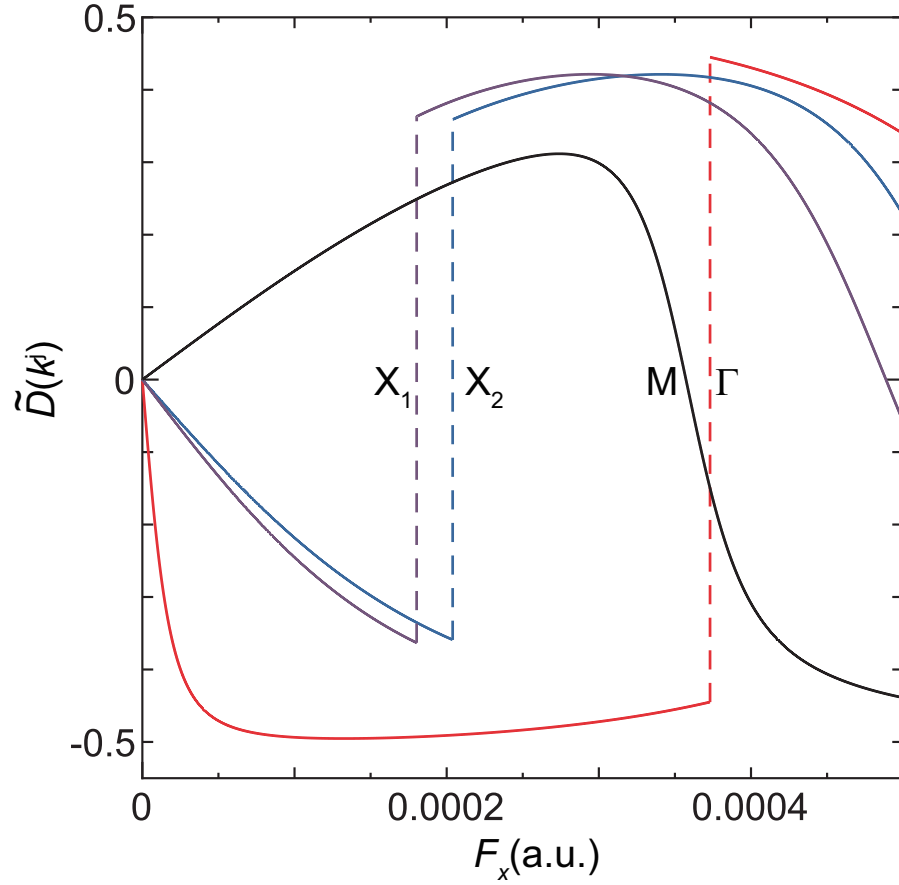


FIG. 7. Variance of interband polarization $\tilde{D}(k^j)$ at high-symmetry points as function of F_x . Interband polarizations at Γ , X_2 , X_1 , and M -points are depicted by red, blue, purple, and black lines, respectively.

Figures

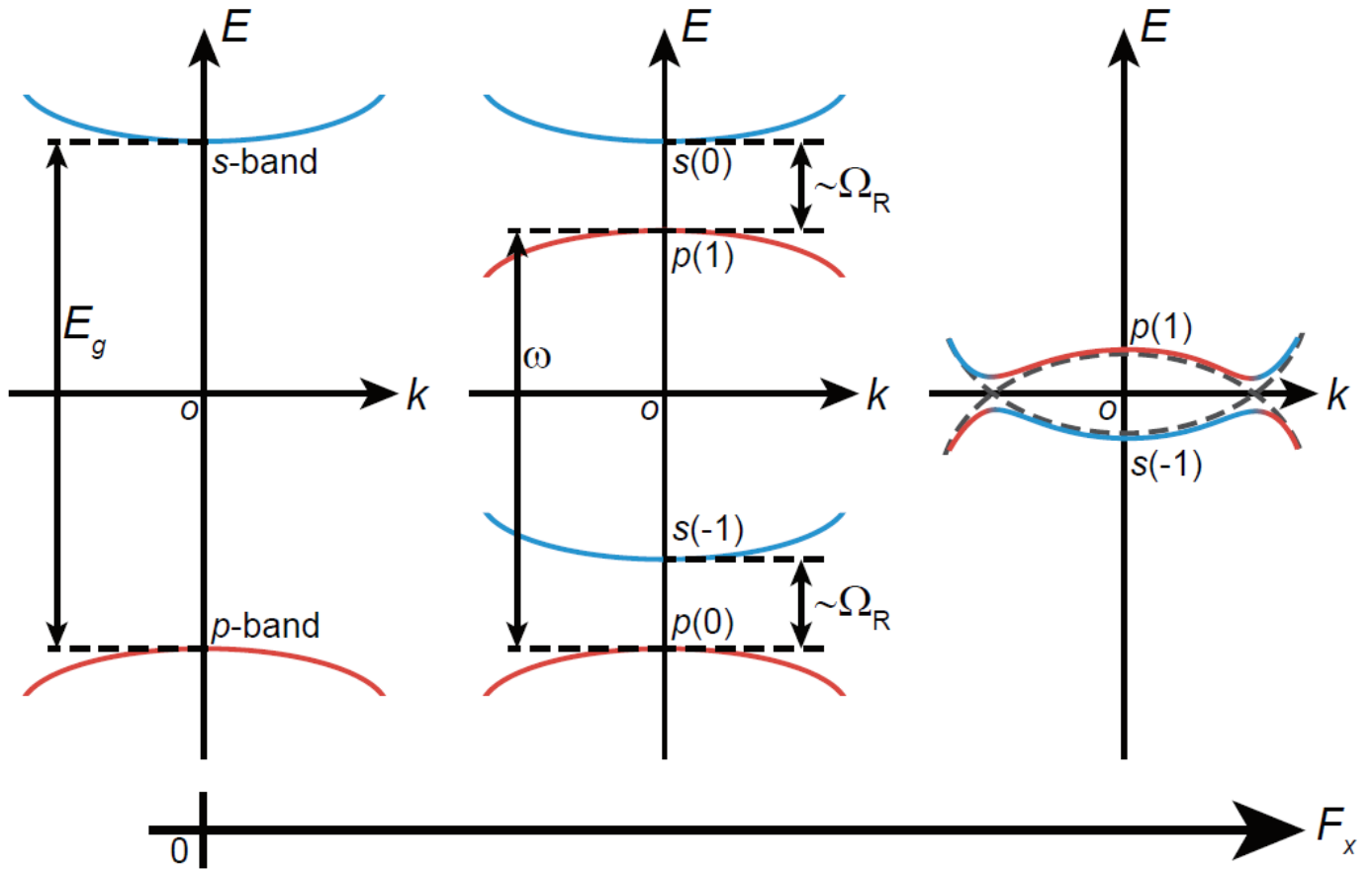


Figure 1

Scheme of the nearly resonant optical-excitation followed by the OSE. (Left) The original energy allocation of the p-band (red solid line) and the s-band (blue solid line) with energy gap E_g . (Center) With the application of cw-laser with frequency ω and constant electric field F_x , the OSE causes quasienergy-splitting of the order of the Rabi frequency Ω_R between a pair of photodressed bands, $s(n \pm 1)$ and $p(n)$, with $n = 0; 1$. (Right) With the further increase in F_x , a pair of bands of $p(1)$ and $s(0)$ undergoes inversion with anticrossing. Band crossing takes place at a certain F_x , as shown by a dashed line.

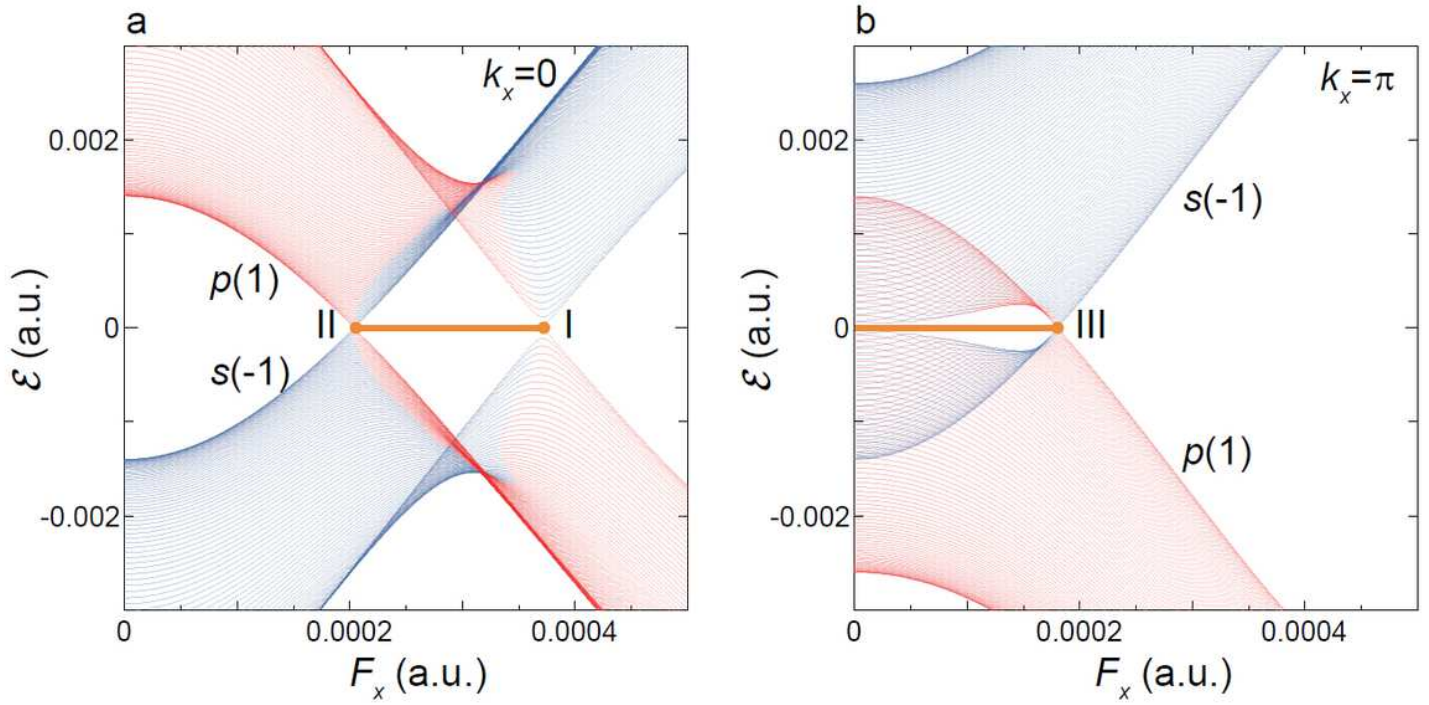


Figure 2

Band inversion and band crossing. (a) Shown are $E_{p(1)}(k_x)$ and $E_{s(-1)}(k_x)$ for $k_x = 0$ as a function of F_x . The two quasienergy bands $p(1)$ and $s(-1)$ (shown by red and blue lines, respectively) cross when F_x is fine-tuned at the positions of I and II. Shown are the zero modes (Dirac nodes) by a yellow solid line. (b) The same as the panel (a) but for $k_x = \pi$. The two quasienergy bands cross when F_x is fine-tuned at the position of III.

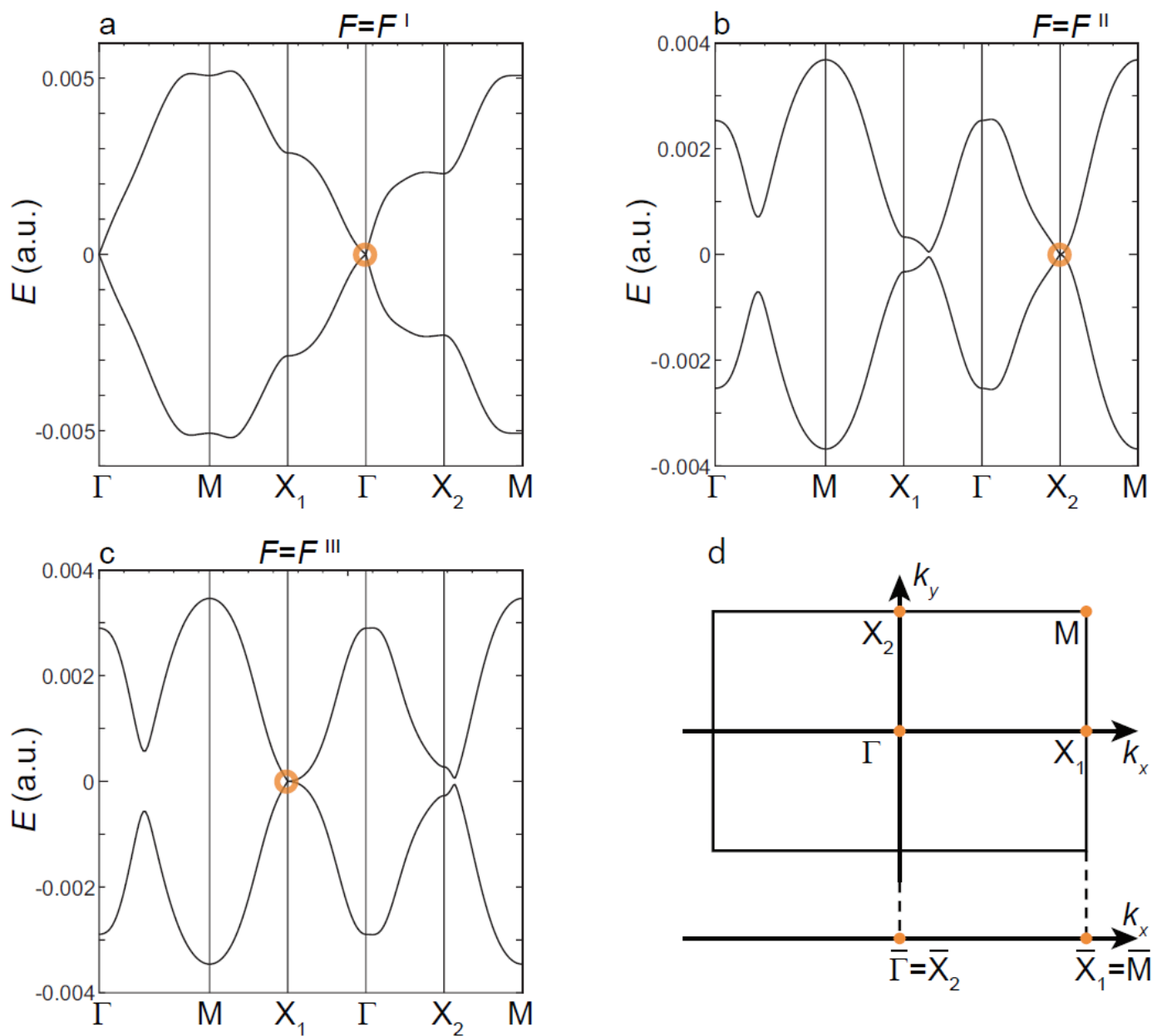


Figure 3

Quasienergy dispersion of 2D-bulk band $E(k)$. (a) Shown is $E(k)$ at F^I , where $E_{p(1)}(k)$ and $E_{s(-1)}(k)$ are degenerate at the Γ point. (b) The same as the panel (a) but at F^{II} with the degeneracy at the X_2 point. (c) The same as the panel (a) but at F^{III} with the degeneracy at the X_1 point. (d) Shown are the high-symmetry points of Γ , X_2 , X_1 and M in the 2D-BZ with their projection onto the k_x -axis denoted as $\bar{\Gamma}$, \bar{X}_2 , \bar{X}_1 and \bar{M} , respectively.

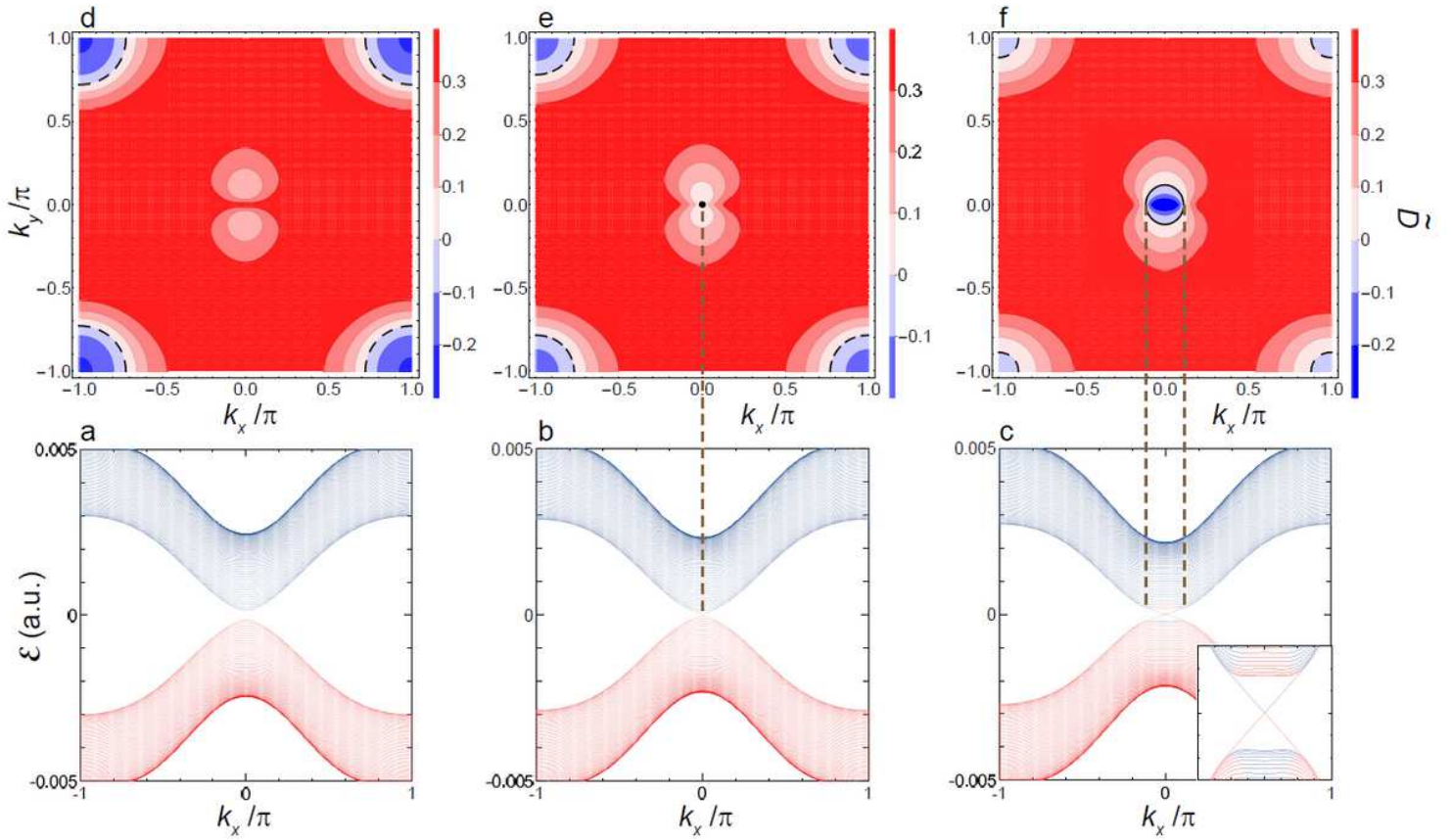


Figure 4

Quasienergy dispersion of $E(k_x)$ and interband polarization $\tilde{D}(k)$ in the vicinity of $F\Gamma_x$. (a) Shown are $E_{p(1)}(k_x)$ and $E_{s(-1)}(k_x)$ as functions of k_x at $F_x > F\Gamma_x$. The two quasienergy bands $p(1)$ and $s(-1)$ are shown by red and blue lines, respectively. (b) The same as the panel (a) but at $F\Gamma_x$. (c) The same as the panel (a) but at $F_x < F\Gamma_x$. Inset: the expanded view of these two bands in the vicinity of the Γ -point. (d) Shown is a contour map $\tilde{D}(k)$ in the (k_x, k_y) -plane at $F_x > F\Gamma_x$. Contours indicating the boundary of $\tilde{D}(k) = 0$ are shown by black dashed lines. (e) The same as the panel (d) but at $F\Gamma_x$. Besides, a pinhole indicating $\tilde{D}(k) = 0$ at the Γ -point is shown by a black filled circle. The vertical dashed line shows the projection of $\tilde{D}(k) = 0$ (the pinhole) onto the k_x -axis shown in the panel (b). (f) The same as the panel (d) but at $F_x < F\Gamma_x$. Contours indicating the boundary of $\tilde{D}(k) = 0$ are shown by black solid and dashed lines. The vertical dashed lines show the projection of $\tilde{D}(k) = 0$ (the zero contour) onto the k_x -axis shown in the panel (c).

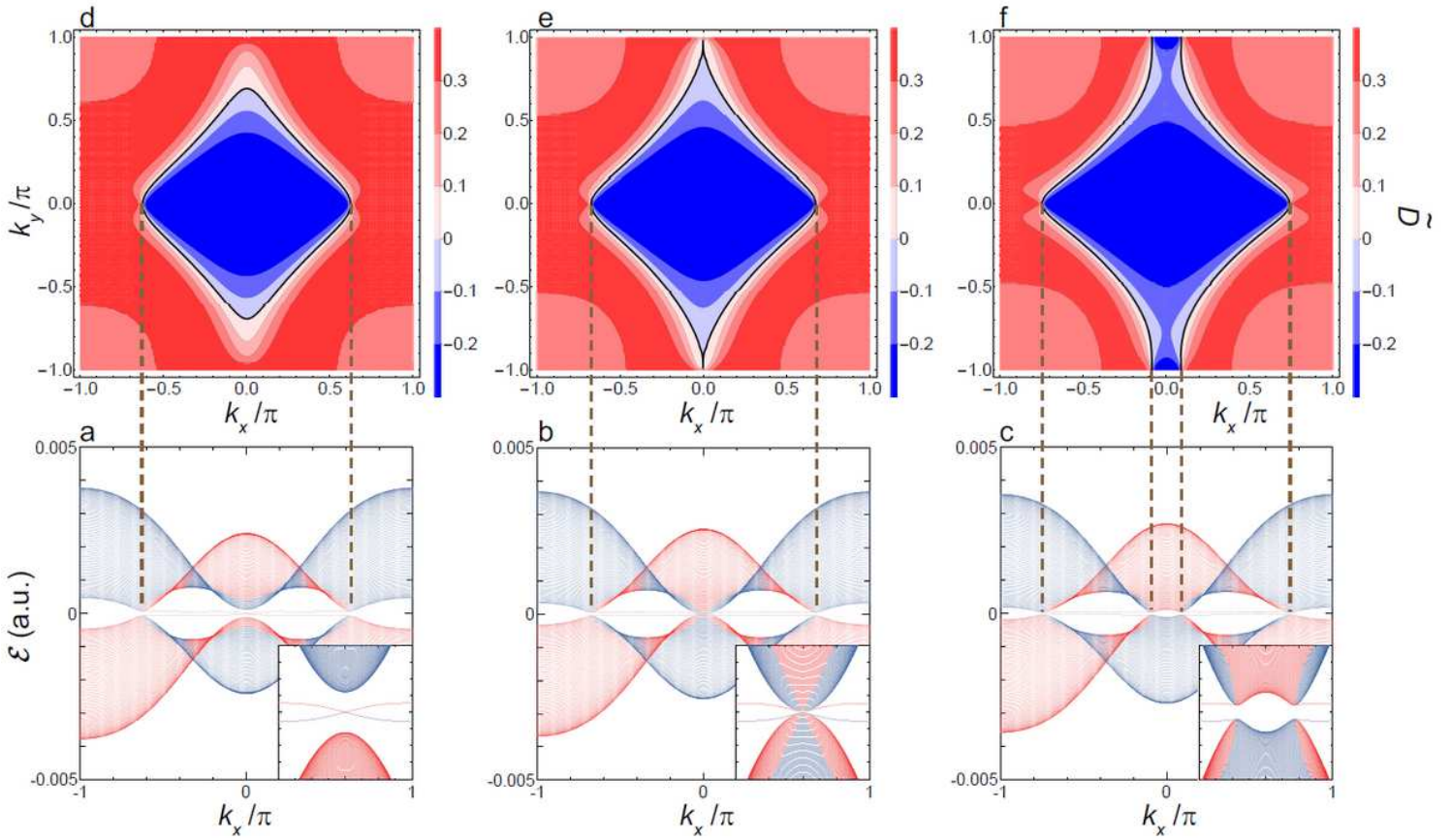


Figure 5

Quasienergy dispersion of $E(\mathbf{k})$ and interband polarization $\tilde{D}(\mathbf{k})$ in the vicinity x . (a) Shown are $E_{p(1)}(\mathbf{k})$ and $E_{s(-1)}(\mathbf{k})$ as functions of k_x at $F_x > F_{X^2}$ of $F_{X^2} x$. The two quasienergy bands $p(1)$ and $s(-1)$ are shown by red and blue lines, respectively. Inset: the expanded view of these two bands in the vicinity of the X^{-2} -point. (b) The same as the panel (a) but at x . (d) Shown is a contour map $\tilde{D}(\mathbf{k})$ in the x . (c) The same as the panel (a) but at $F_x < F_{X^2}$ of $F_{X^2} x$. The vertical dashed lines show the projection of $\tilde{D}(\mathbf{k}) = 0$ (the zero (k_x, k_y) -plane at $F_x > F_{X^2}$ contour) onto the k_x -axis shown in the panel (a). (e) The same as the panel (d) but at $F_{X^2} x$ and with the zero contour projected onto the k_x -axis shown in the panel (b). (f) The same as the panel (d) but at $F_x < F_{X^2}$ of $F_{X^2} x$ and with the zero contour projected onto the k_x -axis shown in the panel (c).

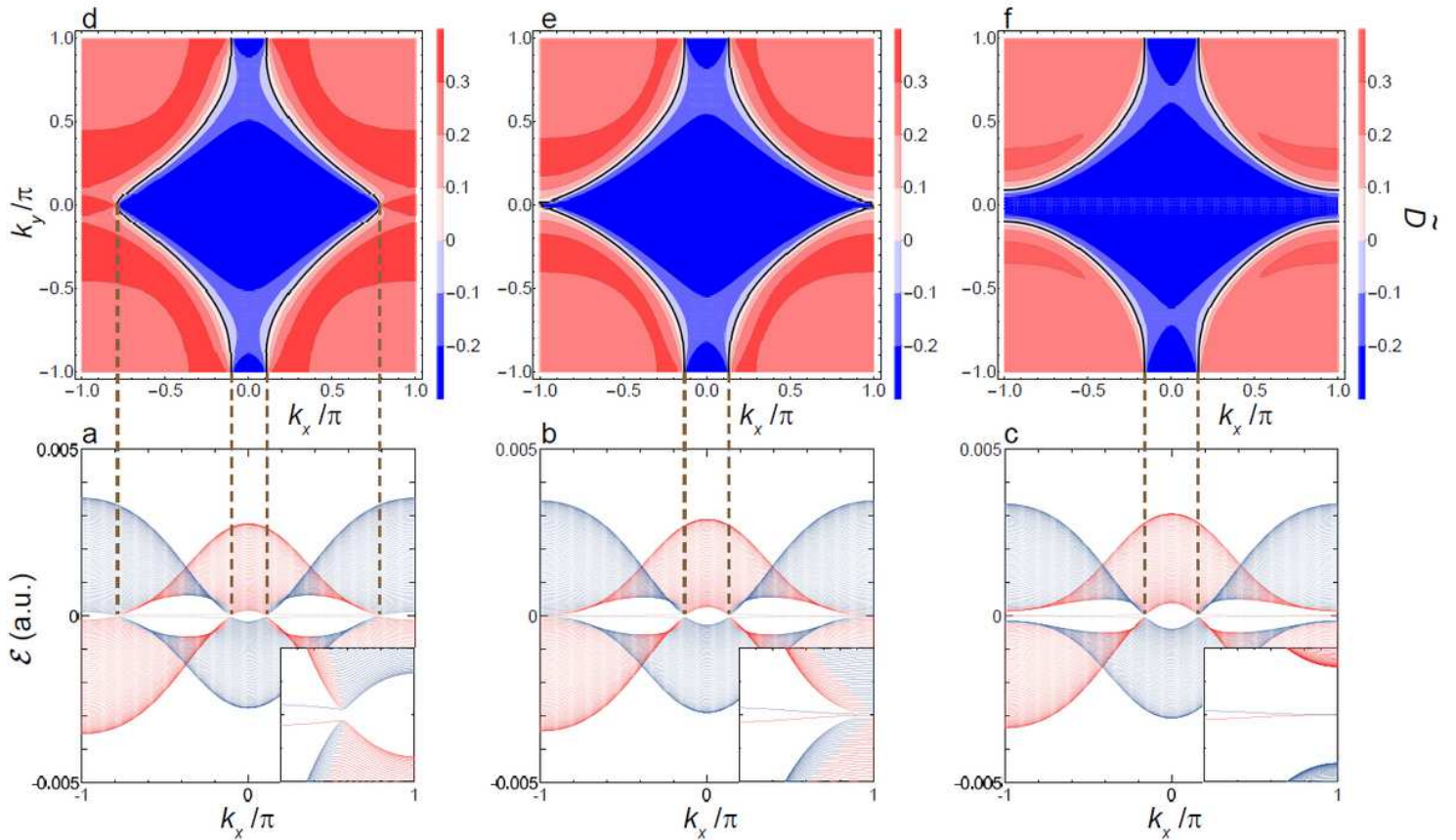


Figure 6

Quasienergy dispersion of $E(\mathbf{k})$ and interband polarization $\tilde{D}(\mathbf{k})$ in the vicinity x . (a) Shown are $E_p(1)(k_x)$ and $E_s(-1)(k_x)$ as functions of k_x at $F_x > F_{X1}$ of F_{X1} x . The two quasienergy bands $p(1)$ and $s(-1)$ are shown by red and blue lines, respectively. Inset: the expanded view of these two bands in the vicinity of the X^{-1} -point. (b) The same as the panel (a) but at x . (d) Shown is a contour map $\tilde{D}(\mathbf{k})$ in the x . (c) The same as the panel (a) but at $F_x < F_{X1}$ F_{X1} x . The vertical dashed lines show the projection of $\tilde{D}(\mathbf{k}) = 0$ (the zero (k_x, k_y) -plane at $F_x > F_{X1}$ contour) onto the k_x -axis shown in the panel (a). (e) The same as the panel (d) but at F_{X1} x and with the zero contour projected onto the k_x -axis shown in the panel (b). (f) The same as the panel (d) but at $F_x < F_{X1}$ x and with the zero contour projected onto the k_x -axis shown in the panel (c).

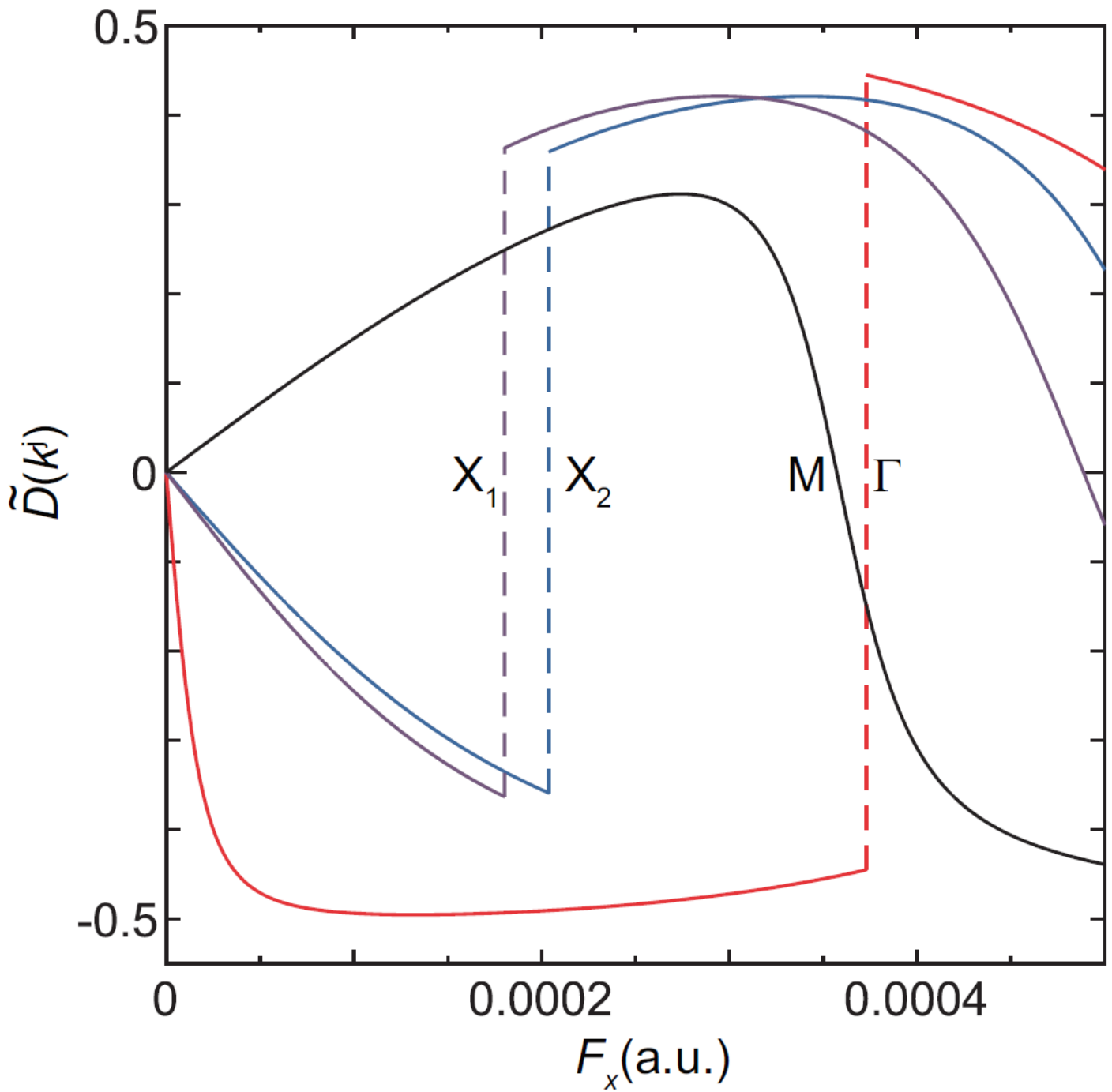


Figure 7

Variance of interband polarization $\tilde{D}(k_i)$ at high-symmetry points as function of F_x . Interband polarizations at Γ , X_2 , X_1 , and M -points are depicted by red, blue, purple, and black lines, respectively.

Supplementary Files

This is a list of supplementary files associated with this preprint. Click to download.

- [FDSMSIR.pdf](#)